Drop Coalescence through a Liquid/Liquid Interface

Zulfaa Mohamed-Kassim, Ellen K. Longmire

Department of Aerospace Engineering and Mechanics, University of Minnesota, Minneapolis, MN 55455, USA

PIV experiments were conducted to study the coalescence of single drops through planar liquid/liquid interfaces. Sequences of velocity vector fields were obtained with a high-speed video camera and subsequent PIV analysis. Two ambient liquids with different viscosity but similar density were examined resulting in Reynolds numbers based on a surface tension velocity of 10 and 26. Prior to rupture, the drops rested on a thin film of ambient liquid above an underlying interface. After rupture, which was typically off-axis, the free edge of the thin film receded rapidly allowing the drop fluid to sink into the bulk liquid below. Vorticity generated in the collapsing fluid developed into a vortex ring straddling the upper drop surface. The ring core traveled radially inward with a ring-shaped capillary wave effectively pinching the upper drop surface and increasing the drop collapse speed. The inertia of the collapse deflected the interface downward before it rebounded upward. During this time, the vortex core split so that part of its initial vorticity moved inside the drop fluid while part remained in the ambient fluid above it. A second ring-shaped capillary wave formed along the interface outside of the drop and propagated radially outward during the collapse. Changing the ambient fluid viscosity resulted in several effects. First, the velocity of the receding free edge was smaller for

higher ambient viscosity. Second, the pinching of the upper drop surface caused by the shrinking capillary ring wave was stronger when the ambient viscosity was lower, and this resulted in a higher maximum collapse speed and higher vorticity values in the dominant vortex ring.

PHYSICS AND ASTRONOMY CLASSIFICATION SCHEME

47.55.Dz Drops and bubbles

I. INTRODUCTION

Drop coalescence occurs commonly in many industrial mixing and separation systems as well as in the environment. Individual drops may coalesce with one another or with a larger volume at a relatively flat interface. In this paper, we focus on drops that are initially surrounded by a liquid medium. The surrounding liquid must be driven out of the gap between two fluid bodies before they can coalesce. If the gap width is reduced to sub-micron scale, molecules at the interfaces can rearrange allowing the coalescence to occur. In either the case of colliding drops or the case of a single drop impacting a flat interface, the interaction time must be sufficient for the liquid film in the gap to drain. Otherwise, the volumes will not coalesce.

Recently, a number of experimental studies have been performed on coalescence between colliding drops[1,2,3,4] Yang *et al.*[3] examined the coalescence of equal-sized drops under creeping flow conditions using a four roll mill apparatus. The rollers were controlled to generate combinations of straining and shear flow that drove two drops toward each other. Drops traveling toward each other with a normal offset distance would coalesce only if the initial offset was very small. Then, the drops would contact and rotate about each other over sufficient time that the film between them was able to drain. In addition, the collision had to be gentle: minimal surface deformation supported relatively quick drainage time and eventual coalescence. A quantitative measure to determine coalescence was given by a capillary number Ca such that

$$Ca = \frac{\mu_s G D}{2\sigma}, \tag{1}$$

where μ_s was the surrounding ambient viscosity, G was the flow strain rate, D was the undeformed drop diameter, and σ was the interfacial tension. Coalescence would occur

only if Ca was below a critical value which decreased with increasing offset. Using the same apparatus, Hu *et al.*[4] found that coalescence was inhibited if interfacial tension was reduced by the presence of surfactant on the interface.

In this paper, we focus on drops driven by gravity through a surrounding liquid to interact with a second liquid lying beneath an initially flat interface. Although the drops typically approach the interface with some velocity and internal circulation, the drop velocity and associated vorticity are dissipated well before the drops coalesce. This behavior is in sharp contrast to that observed for drops falling through gases onto liquid surfaces where coalescence occurs immediately after impact, and thus the initial drop motion and kinetic energy have profound effects on the resulting flow outcome and topology.[5,6,7,8,9,10] The initial conditions in the liquid/liquid flow thus consist of a non-spherical drop suspended above a deformed interface. Between the drop and the interface is a thin film of liquid that must drain radially outward prior to drop rupture. In contrast to the case of colliding drop pairs, the film is not planar, but curved into a lens-like shape.

A number of previous studies have attempted to model the time required for film drainage where typically the drainage was assumed to be axisymmetric[11,12,13,14] In a computational study based on a boundary integral method, Chi and Leal[15] found that, for a low Reynolds number flow (Re << 1), the radial variation in film thickness depended mostly on the viscosity ratio λ between the drop and the surrounding liquid. Re was defined as

$$\mathrm{Re} = \frac{\rho_s U_c D}{2\mu_s}, \tag{2}$$

where ρ_s was the ambient density and U_c was the terminal Stokes velocity. They reported that the film was thinnest at the center for $\lambda = 0.1$, approximately uniform for $\lambda = 1.0$, and

thinnest at a rim of finite radius for $\lambda = 10$. In experimental studies, Hartland found that rupture occurred near the rim, which was the thinnest point within the film, when $\lambda = 4.76$ and 45.9 (drops ruptured near the film center only twice out of more than 100 experiments).[16] Sometimes, a secondary minimum in film thickness occurred at the center especially with large drops.[17]

When the drop eventually ruptures, its outer surface connects to the underlying interface yielding a ring-shaped edge of thin film with a very small radius of curvature. This edge generates a large capillary pressure of order $4\sigma/h_f$ where h_f is the local thin film thickness. The capillary pressure thus causes a rapid retraction of the remaining film. Hartland measured the film retraction speed for $\lambda = 4.76$ and 45.9. He found that the measured speed could be modeled reasonably well by equating interfacial tension with viscous forces.[17] Charles and Mason[18] measured the film retraction speed for $\lambda = 1.48$ showing that it decreased with increasing radius of the hole created by the expanding thin film edge. The behavior of the retracting film in liquid/liquid flow contrasts with outward jetting behavior in liquid/gas flows that has been observed computationally[8] and experimentally[10]. Thoroddsen concluded that the jet originated from the underlying liquid layer and not the drop liquid.[10] In the liquid/gas flows, the dominant mechanism in generating the outward jetting behavior was inertia (as opposed to capillary forces). Weiss and Yarin found that significant capillary forces compared with inertial forces would act to suppress jetting and instead influence outward stretching in the neck region between the drop and the bulk liquid.[8]

When relatively dense drop fluid collapses into the underlying ambient, baroclinic vorticity should be generated. Also, the collapsing interface will generate vorticity of the

same sign. Vortex ring formation was observed in experimental studies of initially stationary drops collapsing in gas/liquid flows[19]. Also, Anilkumar *et al*.[20] observed drops falling through an immiscible liquid before resting on and eventually rupturing at a liquid/liquid interface. In their flow, the fluids and drop size were chosen such that the potential energy associated with the drop fluid immediately after rupture was less than 6% of the surface energy. The drop fluid was observed to form a vortex ring that penetrated to a certain depth below the remaining interface. The measured penetration depths agreed well with predictions based on an energy balance between surface and viscous forces.

Additional studies on drops falling through gases and penetrating into underlying liquids have discussed mechanisms for vortex ring formation associated with the penetration. Thomson and Newall[21] postulated that a vortex film existed across the drop surface during the coalescence; the vortex film then diffused into the surrounding liquid forming the vortex ring. However, there was no mention of how the vorticity was initiated in the first place. Chapman and Critchlow[22] suggested that vorticity was generated due to normal pressure gradients (as a result of surface tension effects) that accelerated the drop downward. Peck and Sigurdson[23] later pointed out that a kinematic condition was required across the boundary layer next to an interface for a jump in vorticity ($\Delta\omega$). In steady flow, the condition is given by

$$\Delta\omega = 2\kappa q \tag{3}$$

where κ is the surface curvature and q is the tangential fluid velocity. Based on this boundary condition, Creswell and Morton[24] argued that as the drop impacted and penetrated into the receiving liquid through an 'opened' contact region, the curved drop

surface 'turned' the moving drop fluid towards the contact region. Here, the curved streamline generated vorticity to maintain zero viscous stress at the free surface. Since the penetration occurred immediately at impact, the velocity jump between the drop fluid and the receiving fluid had to be on the order of the impact velocity, which in turn determined the amount of vorticity generated. We are not aware of any experiments where a vorticity field associated with a penetrating and collapsing drop has been measured.

In the current investigation, the objective was to determine the velocity and vorticity fields through coalescence events in order to quantify the generation and evolution of vorticity as well as to provide test cases for numerical simulations that attempt to simulate the coalescence process. The Particle Image Velocimetry (PIV) method was employed to determine vertically-planar velocity fields of drops surrounded by liquid ambients that underwent coalescence. Our high-speed video camera was able to track the extremely rapid thin film retraction following rupture and the interfacial deformation during drop fluid collapse into the underlying liquid. Velocity field data permitted quantification of vortex ring formation, flow evolution, and vorticity evolution through the coalescence process. With the exception of measurements made in a microscale flow[25], we believe these data are the first to quantify local velocities within drop fluid during a coalescence event.

II. EXPERIMENTAL METHODS

A. Facilities

A transparent glass tank of 40 cm square cross section and 30 cm height was used in our experiment (see Fig. 1). The large tank cross section was important to ensure that reflections of any interfacial waves on the walls were negligible. The tank was filled with two layers of fluid: a mixture of distilled water and glycerin underneath, and a layer of silicone oil (Dow Corning 200® Fluid) on top. The depths of the water/glycerin and silicone oil layers were 13 cm and 10 cm, respectively. In order to study the effect of ambient fluid viscosity, two types of silicone oil with viscosities of 20 cs and 50 cs were used. The drop liquid was identical to the water/glycerin mixture in the large tank. To eliminate optical distortions in photographic imaging, the refractive indices of the mixture and the silicone oil were matched. The matching was achieved to within 0.03% of the index value by controlling the amount of glycerin added to the water. Measurements of the liquid properties are discussed in more detail in a separate paper[26]. Small seed particles of titanium dioxide (1 μm diameter, 3.5 g/cm^3 density) were mixed into all liquids to 'track' the fluid motion in the PIV experiments. The drop was dyed with a very small amount of Rhodamine 6G to make it visible against both bulk liquids. The bulk layer of water/glycerin was dyed with a smaller concentration of Rhodamine 6G. Table I lists the properties of the various liquids used.

Drops were generated through a small cylindrical glass tube placed above the oil/air surface as shown in Fig. 1a. A relatively large drop (D = 1.03 ± 0.015 cm) was created by releasing the drop liquid trapped inside the glass tube. The tube end was located just above the oil surface, but the drop fluid extended beyond the tube end and contacted the

ambient liquid. Once released, the drop descended through the oil layer, eventually reaching a terminal velocity (U_t) of 9.8 cm/s and 13.2 cm/s in the higher and lower viscosity ambient respectively, before impacting on the liquid/liquid interface. The impacting drop oscillated once on the interface before settling to a rest position[26]. During the 'rest period', a thin film of ambient oil beneath each drop drained outward. When the liquids were seeded, the mean rupture time occurred approximately 30 seconds after impact for drops surrounded by the lower viscosity ambient and 60 seconds after impact for drops surrounded by the higher viscosity ambient. The time before coalescence was approximately one fourth the time observed for unseeded fluid cases. These results suggested that the seed particles promoted earlier coalescence by bridging the gap between the bounding interfaces. Individual coalescence times were somewhat unpredictable and varied from event to event.

In order to obtain high-quality images near the bulk liquid/liquid interface, a closed-loop peristaltic pump was used to 'clean' seed particles from the interface before each PIV experiment. Nevertheless, some particles settled onto the bulk and drop surfaces during each experimental run. Typically, a large number of runs were completed for a given case, and those with smaller surface seeding were chosen for PIV processing.

To capture the fluid motion, we utilized a high-speed digital video camera (NAC Memrecam c.i. with 572 x 432 pixel array) and a pulsed Nd:YLF laser. A vertically planar cross-section passing through the drop center was illuminated with a thin laser sheet (thickness $\approx$ 1 mm) formed through a set of spherical and cylindrical lenses. The laser and the camera were synchronized and operated at 500 Hz. Both the laser sheet and camera were inclined upward to illuminate and view, respectively, the drop from

below (see Fig. 1a-b). This arrangement eliminated optical distortions near the bulk interface caused by small variations in the refractive indices. An important feature of the video camera is its continuously updated recording buffer. The camera could be triggered to store a sequence of images recorded before, during, or after any event. Since the time of rupture was somewhat unpredictable, we were able to capture the rupture process by triggering after the event.

B. Experiments and PIV parameters

Two camera objectives were used to obtain low and high magnification images of the drop and its surrounding liquids (the image sizes are tabulated in Table II). The low magnification images showed the flow dynamics away from the drop while the high magnification images allowed us to investigate the evolution of a vortex ring within the drop. Local velocity vectors were obtained by cross-correlating small interrogation areas in two consecutive images, separated by a time difference (Δt) of 2 ms, using *PIV Sleuth* software[27]. For the low magnification experiments, an interrogation area of 32 x 32 pixels (1.7 x 1.7 mm) was chosen with 50% overlap yielding a vector spacing of 16 pixels. For the high magnification experiments, initial vectors were obtained using interrogation areas of 64 x 64 pixels with 75% overlap. Then, the image was re-interrogated using smaller interrogation areas of 32 x 32 pixels (0.84 x 0.84 mm) with 50% overlap. The second interrogation was computed iteratively based on the initial vectors. Once the velocity vectors were obtained, spatial velocity gradients and vorticity were computed based on a three-point central-difference method.

For the low magnification experiments, the total uncertainty in calculating a velocity vector was $0.053U_\sigma$ and $0.051U_\sigma$ for the lower and higher ambient viscosity,

respectively (see Section III.A for a definition of U_σ). For the high magnification experiments, the total uncertainty in calculating a velocity vector was $0.026U_\sigma$ and $0.025U_\sigma$ for the lower and higher ambient viscosity, respectively. The total uncertainty in calculating a velocity vector was dominated by uncertainty in Gaussian peak-fitting during cross-correlation. Other contributors were uncertainty in the magnification measurements and the slight camera inclination. Since the camera was inclined at an angle, the vertical velocity measurement could be affected by flow perpendicular to the laser sheet plane. However, the out-of-plane velocity was very small except near the collapsing drop axis if the sheet were misaligned (see Section III.C for details). We estimated that the maximum out-of-plane velocity yielded an uncertainty of $0.04U_\sigma$. However, this occurred only when the drop collapse rate was at a maximum in the lower viscosity ambient (otherwise, the out-of-plane uncertainty was negligible compared to the peak-fitting uncertainty). This uncertainty was based on a possible laser sheet misalignment of 0.5 mm from the drop center.

The 'in plane' velocity measurements could also be affected by the large velocity (> 100 cm/s) of the receding interface edge during rupture. First, the relatively long Δt of 2 ms could not resolve this large velocity. Second, out-of-plane motion of the receding free edge could make in-plane PIV measurements impossible at that location. In our analysis, the calculated velocity vectors at these locations were often considered as 'bad'. These bad vectors were eliminated and corrected using either additional correlation peaks or interpolation.[26] We encountered at most 3% bad vectors per image occurring mainly near the receding film edge and near the upper drop surface during coalescence where strong

gradients were present. The bad vectors were found mostly before the upper drop surface reached its maximum collapse speed (defined in Section III.C).

III. RESULTS AND DISCUSSION

A. Governing Parameters

In Table III, important parameters for the drop coalescence experiments are presented. The subscript *d* represents the drop liquid while the subscript *s* represents the surrounding silicone oil. A characteristic coalescence velocity, $U_\sigma = D/t_\sigma$, is derived using a time scale based on the surface tension force, where

$$t_\sigma = \sqrt{\frac{\rho_d D^3}{\sigma}}\,. \tag{4}$$

The key difference between the two experimental cases is the viscosity ratio $\lambda = \mu_d/\mu_s$. A measure of the ratio of inertial to viscous forces is given by a surface tension Reynolds number (Re) defined as

$$\mathrm{Re} = \frac{\rho_s U_\sigma D}{\mu_s}\,. \tag{5}$$

Due to varying drop diameters in different experimental runs, an average volume-equivalent spherical drop diameter D of 1.03 ± 0.015 cm is used to represent the results. In the results presented below, length is scaled with D, time with t_σ, and velocity with U_σ.

B. Scaling Analysis

In contrast to the experiments examining water drops in air that impact and coalesce instantaneously, the drop in our experiment is essentially motionless prior to rupture. Fig. 2 shows an idealized drop resting on a deformable interface prior to rupture. After

rupture, the remaining deformed interface as well as the excess potential energy of the drop fluid act to accelerate the drop fluid downward. If the capillary and gravitational effects are scaled as $4\sigma/D$ and $0.5(\rho_d - \rho_s)gD$ respectively, the ratio of capillary to gravitational effects in our experiments is approximately 1.3. During the coalescence process, the capillary effect becomes more significant as the local surface curvature of the remaining drop surface increases. At $0.25t_\sigma$, the local capillary pressure below the upper drop surface increases to about 2.6 and 5.1 times the initial value predicted by $4\sigma/D$ for the lower and higher λ cases, respectively.

C. Interfacial Deformation and Flow Evolution

Figs. 3a-d show raw PIV images from high magnification experiments immediately before, during, and after rupture for $\lambda = 0.33$ (the image brightness has been enhanced for clarity). (Movies of complete image sequences can be observed by accessing the EPAPS files accompanying this article). The interface beneath the drop appears as a bright curve because of extra seed particles settling on the interface. Rupture can be seen in Fig. 3b where a spot beneath the drop suddenly becomes brighter than in the preceding image (this spot is brighter most likely because particles are pushed into the laser plane by a receding interface that ruptured out of the plane). In the measurement plane, the free edge of the film beneath the drop then expands radially outward allowing the drop fluid to collapse into the bulk liquid. This process can be seen in Fig. 3c where bright seed particles bordering the interfaces recede. The maximum velocity of the receding film edge was measured as $\sim 20U_\sigma$ for $\lambda = 0.14$ and $\sim 40U_\sigma$ for $\lambda = 0.33$ (the main cause of this difference is the ambient viscosity). This maximum velocity occurs immediately after

rupture, as the film velocity decreases significantly during the radial expansion. The measured values are lower than those of Charles and Mason[18] who measured maximum speeds of up to $67U_\sigma$ in their liquid/liquid coalescence experiments on water drops in benzene (λ = 1.5; the viscosities of water and benzene were 0.01 g/cm.s and 0.0067 g/cm.s, respectively, which are significantly lower than our values). In Hartland's experiment[16], the speeds were much lower ($0.04U_\sigma$ and $0.6U_\sigma$), apparently due to very large drop viscosities of 78 g/cm.s and 8.1 g/cm.s respectively and a large ambient viscosity of 1.7 g/cm.s.

The motion of the receding edge must shear a layer of water/glycerin fluid immediately above and below it. A first approximation of the maximum shear layer thickness δ can be determined based on Stokes' First Problem (a plate suddenly set in motion in a quiescent fluid) as

$$\delta = 3\sqrt{\nu T} \tag{6}$$

where $T \approx 2$ ms is the estimated time scale over which the process occurs. The resulting thickness δ is less than 1 mm (0.95 mm and 0.6 mm) for both cases. Once the thin film completely disappears, the circular rim connecting the drop and the bulk interface moves outward due to its high local surface curvature (see Figs. 3c and 3d).

In Figs. 4 and 5, the outlines of the drop fluid boundary and the interface obtained from the low magnification experiments are shown sequentially for the two viscosity ratios, λ = 0.14 and λ = 0.33 (the sizes of the images are tabulated in Table II). Prior to rupture, the line between the drop and the interface represents the thin film between them. Immediately after rupture, the break in the line shows the interfacial opening created as the free edge of the film recedes (Figs. 4b and 5b). In the remaining images, the interface

between the drop and the lower fluid has disappeared completely, but the drop fluid boundary is marked by a dashed line. To obtain these outlines, the drop and bulk interfaces from the actual PIV images were marked with small dots. Then, using *Matlab* software, curves were fit through the dots with cubic smoothing spline functions. In Fig. 6, the normalized height of the upper drop surface on the centerline relative to the quiescent interface location, h_u, is shown for both viscosity ratios. The corresponding rate at which h_u decreases is given by $V_u = -\mathrm{d}h_u/\mathrm{d}(t/t_\sigma)$.

Prior to rupture, the drop shapes are identical for both viscosity ratios (Figs. 4a and 5a). Earlier PIV experiments[26] showed that the fluids inside the drop and in the surrounding ambients were motionless prior to rupture (the motion within the film beneath the drop was not resolved). Once the film separating the drop and the interface reaches a critical thickness, rupture occurs at the lower drop surface but usually off-axis (Figs. 4b and 5b). The rate at which h_u decreases immediately after rupture is similar for both viscosity ratios until t/t_σ reaches 0.15. Beyond this time, h_u continues to decrease for $\lambda = 0.14$, while for $\lambda = 0.33$, h_u stays approximately constant until $0.2t_\sigma$. Then, h_u decreases more rapidly for $\lambda = 0.33$ than for $\lambda = 0.14$. The differences in behavior can be explained from the images in Figures 4 and 5. Once the drop surface and the bulk interface become connected, surface tension pulls the kinked portion outward while the drop fluid collapses slowly (see Figs. 4c and 5c); this behavior generates two ring-shaped capillary waves propagating in opposite radial directions (the arrows in Figs. 4c, 4e, 5c, and 5e indicate the kinks associated with the capillary waves). One wave propagates radially outward along the bulk interface at an average velocity of approximately $2.6U_\sigma$ in both cases. The other wave propagates radially inward along the upper drop surface

from the drop outer edge toward the drop centerline. The average propagation velocity of this wave is approximately $1.9U_\sigma$ ($\lambda = 0.14$) and $2.3U_\sigma$ ($\lambda = 0.33$). This motion pinches the upper drop surface into a peak first hindering the collapse of fluid near the centerline (see Figs. 4d, 4e, 5d, and 5e). The interfacial peak caused by the wave is more pronounced in the lower viscosity ambient (see Figs. 4f and 5f). In the higher viscosity ambient, viscous forces tend to damp the capillary wave. The pinching of the upper drop surface increases the local surface curvature (hence the surface tension force), and then accelerates the centerline fluid downward. As a result, V_u subsequently increases for both viscosity ratios. For $0.2 < t_\sigma < 0.32$, V_u is larger for $\lambda = 0.33$ (see Fig. 6). The maximum value of V_u is measured as $8.0U_\sigma \pm 0.4U_\sigma$ at $0.30t_\sigma$ for $\lambda = 0.33$ and $3.7U_\sigma \pm 0.4U_\sigma$ at $0.33t_\sigma$ for $\lambda = 0.14$.

The inertia of the collapsing fluid continues to deflect the interface downward until a maximum deflection is reached (see Figs. 4g and 5g). This deflection is measured as $0.17D$ ($\lambda = 0.14$) and $0.24D$ ($\lambda = 0.33$). The subsequent rebound of the interface creates another ring wave propagating radially outward. The surface centerline finally settles at the quiescent interface level at approximately $1.3t_\sigma$ for both λ cases (see Figs. 4h and 5h). However, the leading edge of the drop fluid continues to sink slowly downward at approximately $0.10U_\sigma \pm 0.02U_\sigma$ and $0.14 \pm 0.02U_\sigma$ with the higher and lower viscosity ambient, respectively (see the accompanying EPAPS movie files to observe this behavior).

Normalized vertical velocity v/U_σ contours are shown in Figs. 7a-d ($\lambda = 0.14$) and 7e-h ($\lambda = 0.33$). The PIV results show that the drop fluid accelerates downward immediately after coalescence until V_u reaches a maximum value as described above (see

Figs. 7a-c and 7e-g; note that the contour levels shown extend to magnitudes of $1.0U_\sigma$ only). The maximum downward velocity reaches $0.8U_\sigma$ at $0.05t_\sigma$ for both viscosity ratios (see Figs. 7a and 7e). At $0.15t_\sigma$, this velocity magnitude increases to $1.2U_\sigma$ and $1.5U_\sigma$ for the lower and higher λ cases, respectively. Meanwhile, the interfaces near the drop fluid outer rim are moving upward due to the expanding capillary wave. These upward moving interfaces are also expanding outward as shown in Figs. 7b-d (λ = 0.14) and Figs. 7f-h (λ = 0.33). The interface centerline reaches its maximum downward deflection at $0.44t_\sigma$ in the lower viscosity ambient. Thus, the fluid near this location is motionless for this case (see Fig. 7h) in contrast to the higher viscosity ambient case where fluid is still moving downward (see Fig. 7d).

Normalized radial velocity u_r/U_σ contours are shown in Figs. 8a-d (λ = 0.14) and 8e-h (λ = 0.33). In general, the drop fluid is pushed radially outward while the ambient silicone oil above the drop is dragged inward toward the centerline. At $0.15t_\sigma$, the maximum outward velocity is $1.0U_\sigma$ for λ = 0.14 and $0.9U_\sigma$ for λ = 0.33 (see Figs. 8b and 8f). This value decreases to $0.9U_\sigma$ for λ = 0.14 and increases to $1.0U_\sigma$ for λ = 0.33 when V_u reaches a maximum value (see Figs. 8c and 8g). The maximum inward velocity, which occurs slightly above the interface, also decreases from $1.0U_\sigma$ to $0.9U_\sigma$ in the higher viscosity ambient between the times $0.15t_\sigma$ and $0.33t_\sigma$. However, this is not the case for the lower viscosity ambient where the value stays approximately constant at $1.2U_\sigma$ between the times $0.15t_\sigma$ and $0.30t_\sigma$. Notice that the radial velocity magnitudes are larger toward the right hand side in most of the fields (see Figs. 8c, 8d, and 8h). This is

consistent with the rupture location that was on the right hand side of both flow sequences (see Figs. 8a and 8e).

In flow visualization experiments, where the fluids were dyed but not seeded, we observed that the sinking drop fluid left behind an elongated neck. In Fig. 9a, which is an unseeded image obtained for $\lambda = 0.14$ at $6.8t_\sigma$, the drop sank along the center axis following a rupture that occurred near the centerline. The bulging drop front is connected to the interface by a trailing neck; this shape is qualitatively similar to those observed by Thomson and Newall[21] and Anilkumar *et al.*[20] A drop sinking asymmetrically at $6.2t_\sigma$ is shown in Fig. 9b ($\lambda = 0.14$) following an off-axis rupture (fortunately, the drop fluid moved within the laser sheet plane which made it visible). In the PIV experiments, the drop fluid usually moved out of the laser plane at longer times such as those shown here.

In a recent study of a stationary drop coalescing through an air/liquid interface by Thoroddsen and Takehara[28], a phenomenon known as partial coalescence was observed. During coalescence, an inward traveling capillary wave caused the formation of a liquid column atop the coalescing fluid. Then, a Rayleigh-type instability caused the column to pinch off above the coalescing fluid. The remaining fluid volume eventually coalesced in a cascade where each step pinched off a smaller drop. In their experiment, λ was approximately 57 ($\mathrm{Re} \approx 32$). Partial coalescence was also observed in a variety of liquid/liquid systems by Charles and Mason who characterized the behavior using viscosity ratio[29]. The smallest viscosity ratio that led to partial coalescence was 0.02 ($\mathrm{Re} \approx 7$) and the largest was 11 ($\mathrm{Re} \approx 443$); however, there were intermediate values of λ for which partial coalescence did not occur. The viscosity ratios in our experiment lie within this range, and we did not observe any partial coalescence. One key difference between

our experiment and Charles and Mason's lies in the absolute values of the drop and ambient liquid viscosities. If we focus on absolute drop viscosity, we can define a Reynolds number based on the drop fluid (Re_d) as

$$\mathrm{Re}_d = \frac{\rho_d U_\sigma D}{\mu_d}. \tag{7}$$

This parameter thus characterizes damping effects of drop viscosity which tend to suppress partial coalescence.[28] In our experiments, Re_d was 88 and 92 for the lower and higher λ cases, respectively. In Charles and Mason's experiments, Re_d was approximately 404 ($\lambda = 0.02$) and 53 ($\lambda = 11$), so again our cases fall between theirs. In Thoroddsen and Takehara's experiment, Re_d was approximately 464. It seems reasonable that higher fluid viscosities (both drop and ambient) would tend to damp the wave motion that results in partial coalescence. Hence, a Reynolds number based on the average of both viscosities might provide a better measure for partial coalescence, where partial coalescence is promoted with the increase of this Reynolds number.

Another factor expected to have a strong influence is the ratio of gravity to surface tension forces. If a Bond number Bo is defined as $(\rho_d - \rho_s)gD^2/\sigma$, increasing Bo should tend to inhibit partial coalescence. This is because the gravitational acceleration of the drop liquid should dominate the capillary pinching of the liquid column. The Bond numbers were 6.0 ($\lambda = 0.14$) and 6.4 ($\lambda = 0.33$) for our two cases and 1.2 for Thoroddsen and Takehara's experiment. In Charles and Mason's experiments, Bond numbers up to 2.8 yielded partial coalescence, but several combinations with lower Bond numbers did not. After further examination of many possible parameter combinations (including Ca for example) applied to 28 cases available from Charles and Mason, Thoroddsen and

Takehara, and our experiments, the best indicator we found for partial coalescence was the ratio Bo/Re_{Av} where Re_{Av} is based on U_σ, D, and the average density and viscosity of both fluids. The value of this ratio ranged from 0.002 to 1.2 for all the cases examined. For $Bo/Re_{Av} < 0.02$-0.03, partial coalescence occurred in all cases, and for $Bo/Re_{Av} > 0.02$-0.03, partial coalescence was suppressed in all cases but one (carbon tetracholoride drops in a 75% glycerine/25% water mixture where $Bo/Re_{Av} = 0.15$)[29]. (We could not find a physical explanation for the lone exception). The overwhelming trend thus shows that the magnitudes of gravitational, surface tension, and viscous forces all play a role in determining whether partial coalescence occurs. Also, our examination of various parameters and the result including average density and viscosity values demonstrate that the properties of both the drop and the surrounding fluid are important in determining the coalescence behavior.

D. Vorticity Generation and Evolution

The velocity vector plots obtained from high magnification experiments immediately after rupture are shown in Figs. 10a ($\lambda = 0.14$) and 10b ($\lambda = 0.33$). In these plots, drop fluid above the thin film moves radially inward and into the bulk liquid below due to the gravitational and surface tension forces described in Section III.B; the drop fluid is sinking at an average speed of approximately $0.3U_\sigma$. In the PIV results, the thin films near the receding free edges are moving upward at approximately the same velocity that the drop fluid is moving downward. At this point, we cannot be certain of why this is happening other than that the interface is moving upward to displace the drop fluid that is flowing downward. In Fig. 10b, the right receding edge reaches the outer rim of the film

connecting the bulk interface with the drop surface; at this point, the highly curved surface of the rim moves outward at a speed of approximately $3.8U_\sigma$. Note that the large crude-looking vectors near the right outer drop surface in Fig. 10b are most likely caused by large velocity gradients within a small area due to the high surface curvature there.

The corresponding normalized vorticity contour plots $\omega_z/(U_\sigma/D)$ are shown in Figs. 11a ($\lambda = 0.14$) and 11b ($\lambda = 0.33$). For interrogation areas without strong velocity gradients, the uncertainty in each vorticity measurement is less than $\pm 1.3U_\sigma/D$. However, because of limitations in both spatial and time resolution, we are not able to resolve the maximum vorticity values generated next to the rapidly receding thin film.

In the plots shown, the collapsing drop fluid near the interfacial opening appears to generate the dominant vorticity cores (the vorticity values may be enhanced by the motion of the receding interface beneath the drop). For $\lambda = 0.14$, the maximum measured vorticity value is about $12U_\sigma/D$ (see Fig. 11a). Note that with finer PIV resolution, this value would probably be higher. The vorticity cores at the receding edges later expand to the outer rim. For $\lambda = 0.33$, the maximum vorticity values inside the drop are $30U_i/D$ near the left receding edge (the levels plotted extend to magnitudes of $20U_\sigma/D$ only), and $49U_\sigma/D$ near the right outer rim. Note that in this case, the interface has retracted further than for $\lambda = 0.14$. Also, for $\lambda = 0.33$, the interface has receded further on the right-hand side than on the left. On the right-hand side of Figure 11b, the strongest core is clearly focused in the drop fluids a small distance away from the interface where the inflection in the local curvature encourages counterclockwise rotation. Outside of this core is an opposing weaker core (maximum value of $20U_\sigma/D$) encouraged by an opposite but

weaker inflection. This core, which must be part of a vortex ring, later expands radially outward along with the outer capillary wave.

The subsequent evolution of normalized vorticity $\omega_z/(U_\sigma/D)$ is shown in Figs. 12a-d for $\lambda = 0.14$ and Figs. 12e-h for $\lambda = 0.33$. The final time in each sequence correlates approximately with the time of maximum V_u. The contour levels are plotted to magnitudes of $40U_\sigma/D$. In Figs. 13a-c ($\lambda = 0.14$) and 13d-f ($\lambda = 0.33$), the normalized vorticity contours are presented during interfacial rebound (the contour levels cover a reduced range).

In both cases, a vortex ring straddles the upper drop surface and contracts radially inward along with the capillary wave mentioned earlier. When the ambient viscosity is lower, the maximum vorticity magnitude occurs when V_u is maximized (see Fig. 12h); the maximum vorticity value is approximately $87U_\sigma/D$. On the other hand, when the ambient viscosity is higher, the maximum vorticity magnitude decreases as V_u approaches a maximum. In this case, the maximum value of ω_z is approximately $34U_\sigma/D$ at $0.15t_\sigma$ (see Fig. 12b) and $25U_\sigma/D$ at $0.33t_\sigma$ (see Fig. 12d).

After the interface center moves below the equilibrium height, the maximum vorticity magnitude decreases due to viscous dissipation. Also, the deflected interface begins to generate vorticity that opposes the dominant vortex ring (this can be seen clearly in Figs. 13b and 13d). The dominant ring begins to split into two – one located above the interface and the other in the drop fluid beneath the interface (see Figs. 13a-f). The maximum ω_z inside the drop is approximately $3U_\sigma/D$ for $\lambda = 0.14$ and $7U_\sigma/D$ for $\lambda = 0.33$ when the interface achieves its maximum downward deflection (Figs. 13c, 13f). When the interface rebounds upward (not shown), the circulation of the lower vortex ring

continues to advect the drop fluid downward. The maximum ω_z inside the drop fluid has decreased to approximately $2U_\sigma/D$ for both cases when the interface finally comes to rest. At the same time, the upper ring of like sign has completely dissipated, and the opposing ring on the interface has a maximum vorticity of approximately $2U_\sigma/D$ for both cases. This ring expands to a diameter of less than $1.0D$. The rotation patterns for both flow cases can also be observed in the EPAPS movies.

IV. SUMMARY AND CONCLUSIONS

PIV experiments were conducted on the rupture and coalescence of a drop through a planar liquid/liquid interface. A high-speed video camera with a closed-loop recording buffer allowed us to record the events before and after rupture in a single sequence and therefore to obtain continuously evolving velocity fields within the drop and the surrounding bulk liquids.

Before rupture, the drops were essentially motionless above the interface. After the interfacial rupture, which was typically off-axis, a capillary force pulled the free edge of the thin film outward at a velocity of more than $20U_\sigma$, rapidly forming a large opening beneath the drop fluid. This opening allowed the drop fluid to sink into the bulk liquid below due to excess pressure inside the drop. Scaling analysis showed that the excess pressure was caused by both gravitational and capillary effects.

Once the receding free edge approached the outer rim, two ring-shaped capillary waves were generated: one that expanded radially outward along the bulk interface and one that propagated radially inward on the upper drop surface. The inwardly propagating

wave generated a peak on the interface near the centerline increasing the local surface tension force and subsequently increasing the collapse speed of the drop fluid. The sharpness of the interface peak and resulting downward acceleration were stronger for the case with lower viscosity fluid above the interface. The maximum downward speed at the center of the interface was $8.0U_\sigma$ for the lower viscosity ambient and $3.7U_\sigma$ for the higher viscosity ambient. The wave behavior observed was similar to that observed in previous experiments on drops rupturing at gas/liquid interfaces[28,29]. A key difference, however, is that in the current experiments, no 'partial coalescence' or formation of secondary drops occurred. This is most likely due to damping of the inward propagating wave by the liquid layer above the interface. The lack of partial coalescence was correlated with relatively high values of $\mathrm{Bo/Re_{Av}}$ (= 0.3 and 0.15) in our cases.

The PIV experiments were not able to fully resolve the initial vorticity generated by the retracting thin film after rupture where the vorticity thickness was estimated as submillimeter. However, they were able to quantify and track the evolution of the dominant vortex ring associated with the collapsing drop fluid. This ring, which first straddled the interface, was centered on the inward-moving capillary wave until it reached the centerline. The maximum vorticity value ($\approx 87U_\sigma/D$) for the case with lower ambient viscosity occurred when the interface centerline reached its maximum collapse speed which coincided approximately with the interface crossing the equilibrium height. On the other hand, in the case with higher viscosity ambient, the maximum vorticity value ($\approx 34U_\sigma/D$) occurred before the interface centerline crossed the equilibrium height. Thus, early dissipation was significant in this case.

In both cases examined, the inertia of the collapse deflected the interface downward before it rebounded upward. The maximum deflection distance was $0.24D$ in the lower viscosity ambient and $0.17D$ in the higher viscosity ambient. During this period, the deformed interface generated vorticity opposing the dominant vortex ring effectively splitting it in two. The opposing vortex ring eventually expanded slightly to a diameter of about 1D. Meanwhile, the dominant ring was split into a stronger core located inside of the original drop fluid and a weaker dissipating core above the opposing ring. The remaining interface eventually came to rest while the drop fluid and the vortex ring within it continued to sink slowly downward. Typically, the drop fluid moved off axis as it sank which was consistent with the original off-axis rupture.

ACKNOWLEDGMENTS

This work was supported by the Engineering Research Program of the Office of Basic Energy Sciences at the Department of Energy (Grant DE-FG02-98ER14869). The first author was supported by a Doctoral Dissertation Fellowship from the University of Minnesota Graduate School and a scholarship from Science University of Malaysia. We would like to thank Professor Ronald J. Adrian of the University of Illinois for providing access to the *PIV Sleuth* software.

[1] S. Guido and M. Simeone, "Binary collision of drops in simple shear flow by computer-assisted video optical microscopy," J. Fluid Mech. **357**, 1-20 (1998).

[2] J. W. Ha, Y. Yoon, and L. G. Leal, "The effect of compatibilizer on the coalescence of two drops in flow," Phys. Fluids **15**, 4 (2003).

[3] H. Yang, C. C. Park, Y. T. Hu, and L. G. Leal, "The coalescence of two equal-sized drops in a two dimensional linear flow," Phys. Fluids **13**, 5 (2001).

[4] Y. T. Hu, D. J. Pine, and L. G. Leal, "Drop deformation, breakup, and coalescence with compatibilizer," Phys. Fluids **12**, 3 (2000).

[5] H. N. Oguz and A. Prosperetti, "Bubble entrainment by the impact of drops on liquid surfaces," J. Fluid Mech. **219**, 143-179 (1990).

[6] J. Shin and T. A. McMahon, "The tuning of a splash," Phys. Fluids **A 2**, 8 (1990).

[7] M. Rein, "The transitional regime between coalescing and splashing drops," J. Fluid Mech. **306**, 145-165 (1996).

[8] D. A. Weiss and A. L. Yarin, "Single drop impact onto liquid films: neck distortion, jetting, tiny bubble entrainment, and crown formation," J. Fluid Mech. **385**, 229-254 (1999).

[9] D. Morton, M. Rudman, and L. Jong-Leng, "An investigation of the flow regimes resulting from splashing drops," Phys. Fluids **12**, 4 (2000).

[10] S. T. Thoroddsen, "The ejecta sheet generated by the impact of a drop," J. Fluid Mech. **451**, 373-381 (2002).

[11] G. D. M. MacKay and S. G. Mason, "The gravity approach and coalescence of fluid drops at liquid interfaces," The Canadian J. Chem. Eng. October, 203-212 (1963).

[12] G. Marrucci, "A theory of coalescence," Chem. Eng. Science **24**, 975-985 (1969).

[13] X. B. Reed, Jr., E. Riolo, and S. Hartland, "The effect of hydrodynamic coupling on the axisymmetric drainage of thin films," Int. J. Multiphase Flow **1**, 411-436 (1974).

[14] A. J. S. Liem and D. R. Woods, "Application of the parallel disc model for uneven film thinning," The Canadian J. Chem. Eng. **52**, 222-227 (1974).

[15] B. K. Chi and L. G. Leal, "A theoretical study of the motion of a viscous drop toward a fluid interface at low Reynolds number," J. Fluid Mech. **201**, 123-146 (1989).

[16] S. Hartland, "The coalescence of a liquid drop at a liquid-liquid interface. Part III: film rupture," Trans. I. Chem. Engineers **45**, T109-T114 (1967).

[17] S. Hartland, "The coalescence of a liquid drop at a liquid-liquid interface. Part II: film thickness," Trans. I. Chem. Engineers **45**, T102-T108 (1967).

[18] G. E. Charles and S. G. Mason, "The coalescence of liquid drops with flat liquid/liquid interfaces," J. Colloid Sci. **15**, 236-267 (1960).

[19] P. N. Shankar and M. Kumar, "Vortex rings generated by drops just coalescing with a pool," Phys. Fluids **7**, 4 (1995).

[20] A. V. Anilkumar, C. P. Lee, and T. G. Wang, "Surface-tension-induced mixing following coalescence of initially stationary drops," Phys. Fluids **A3**, 11 (1991).

[21] J. J. Thomson and H. F. Newall, "On the formation of vortex rings by drops falling into liquids, and some related phenomena," Proc. R. Soc. Lond. A **39**, 417-436 (1885).

[22] D. S. Chapman and P. R. Critchlow, "Formation of vortex rings from falling drops," J. Fluid Mech. **29**, 177-185 (1967).

[23] B. Peck and L. Sigurdson, "The three-dimensional vortex structure of an impacting water drop," Phys. Fluids **6**, 564-576 (1994).

[24] R. W. Cresswell and B. R. Morton, "Drop-formed vortex rings – The generation of vorticity," Phys. Fluids **7**, 1363-1370 (1995).

[25] C. Verdier and M. Brizard, "Understanding droplet coalescence and its use to estimate interfacial tension," Rheol. Acta **41**, 514-523 (2002).

[26] Z. Mohamed-Kassim and E. K. Longmire, "Drop impact on a liquid/liquid interface," Phys. Fluids **15**, 3263-3272 (2003).

[27] K. T. Christensen and S. M. Soloff, "*PIV Sleuth*: integrated particle image velocimetry (PIV) interrogation/validation software," Dept. of Theoretical and Applied Mech., U. of Illinois at Urbana Champaign, Technical Report 943 (2000).

[28] S. T. Thoroddsen and K. Takehara, "The coalescence cascade of a drop," Phys. Fluids **12**, 1265-1267 (2000).

[29] G. E. Charles and S. G. Mason, "The mechanism of partial coalescence of liquid drops at liquid/liquid interfaces," J. Colloid Sci. **15**, 105-122 (1960).

TABLE I. Material properties of Dow Corning 200® Fluid, 20 cs and 50 cs, and water/glycerin mixture.

Combination 1			
	Units	20 cs	Water/glycerin
Density, ρ	g/cm^3	0.949	1.128 ± 0.001
Kinematic viscosity, ν	cm^2/s	0.20	0.056 ± 0.001
Dynamic viscosity, μ	g/cm.s	0.19	0.063 ± 0.001
Refractive index, n		1.400	1.400 ± 0.0004
Volume ratio			0.55/0.45
Interfacial tension, σ	mN/m		29.1
Combination 2			
	Units	50 cs	Water/glycerin
Density, ρ	g/cm^3	0.960	1.131 ± 0.001
Kinematic viscosity, ν	cm^2/s	0.50	0.059 ± 0.001
Dynamic viscosity, μ	g/cm.s	0.48	0.067 ± 0.001
Refractive index, n		1.401	1.401 ± 0.0004
Volume ratio			0.54/0.46
Interfacial tension, σ	mN/m		29.5

Table II. Imaging parameters.

Combination 1			
	Units	60 mm lens	105 mm lens
Camera angle	degree	13.9	13.6
Field of view	cm x cm	3.04 x 2.37	1.54 x 1.20
Combination 2			
	Units	60 mm lens	105 mm lens
Camera angle	degree	11.7	10.1
Field of view	cm x cm	2.95 x 2.27	1.47 x 1.13

Table III. Experimental parameters.

	Units	Comb. 1	Comb. 2
Diameter, D	cm	1.03	1.03
Characteristic velocity, U_σ	cm/s	5.00	5.03
Surface tension time scale, t_σ	ms	206	205
Density ratio, ρ_d/ρ_s		1.189	1.178
Viscosity ratio, $\lambda = \mu_d/\mu_s$		0.33	0.14
Reynolds number, Re		26	10

FIG. 1. Side views of camera positioning (top) and laser sheet alignment (bottom). Camera view is normal to laser sheet.

FIG. 2. Idealized drop resting on an interface for scaling analysis.

FIG. 3. Brightness-enhanced raw PIV images from high magnification experiments for $\lambda = 0.33$ showing the rupture process. Image sizes are given in Table II.

FIG. 4. Time evolution of the drop before and after rupture for $\lambda = 0.14$.

FIG. 5. Time evolution of the drop before and after rupture for $\lambda = 0.33$.

FIG. 6. Normalized locations of the upper drop surface on the centerline relative to quiescent interface, h_u, during the coalescence for λ=0.14 (x) and λ=0.33 (o). Measurement errors are less than $\pm 0.01D$.

FIG. 7. Normalized vertical velocity contour plots for $\lambda = 0.14$ (a, b, c, d) and for $\lambda = 0.33$ (e, f, g, h). Spacing between tick-marks on each axis is $1.0D$. The middle tick-mark on the radial axis represents the drop center; the middle tick-mark on the vertical axis represents the quiescent interface. Positive values (upward velocities) are shown with solid lines and negative values with dashed lines.

FIG. 8. Normalized radial velocity contour plots for $\lambda = 0.14$ (a, b, c, d) and for $\lambda = 0.33$ (e, f, g, h). Spacing between tick-marks on each axis is $1.0D$. The middle tick-mark on the radial axis represents the

drop center; the middle tick-mark on the vertical axis represents the quiescent interface. Positive values (outward velocities) are shown with solid lines and negative values with dashed lines.

FIG. 9. Axisymmetric (a) and asymmetric (b) sinking drop fluid obtained from raw images of flow visualization experiments for $\lambda = 0.14$.

FIG. 10. Normalized velocity vector field at $t/t_\sigma = 0.01$ for $\lambda = 0.14$ (a) and for $\lambda = 0.33$ (b). A reference vector of magnitude $1.0U_i$ is placed at the bottom right corner of each image. Spacing between tick-marks on each axis is $0.5D$. The middle tick-mark on the radial axis represents the drop center; the middle tick-mark on the vertical axis represents the quiescent interface.

FIG. 11. Normalized vorticity contour plots for $\lambda = 0.14$ (a) and for $\lambda = 0.33$ (b). Spacing between tick-marks on each axis is $0.5D$. The middle tick-mark on the radial axis represents the drop center; the middle tick-mark on the vertical axis represents the quiescent interface. Positive values (counterclockwise rotation) are shown with solid lines and negative values with dashed lines.

FIG. 12. Normalized vorticity contour plots for $\lambda = 0.14$ (a, b, c, d) and for $\lambda = 0.33$ (e, f, g, h) before maximum h_u collapse speed. Spacing between tick-marks on each axis is $0.5D$. The middle tick-mark on the radial axis represents the drop center; the middle tick-mark on the vertical axis represents the quiescent interface. Positive values (counterclockwise rotation) are shown with solid lines and negative values with dashed lines.

FIG. 13. Normalized vorticity contour plots for $\lambda = 0.14$ (a) and for $\lambda = 0.33$ (b) after maximum h_u collapse speed. Spacing between tick-marks on each axis is $0.5D$. The middle tick-mark on the radial axis represents the drop center; the middle tick-mark on the vertical axis represents the quiescent interface. Positive values (counterclockwise rotation) are shown with solid lines and negative values with dashed lines.

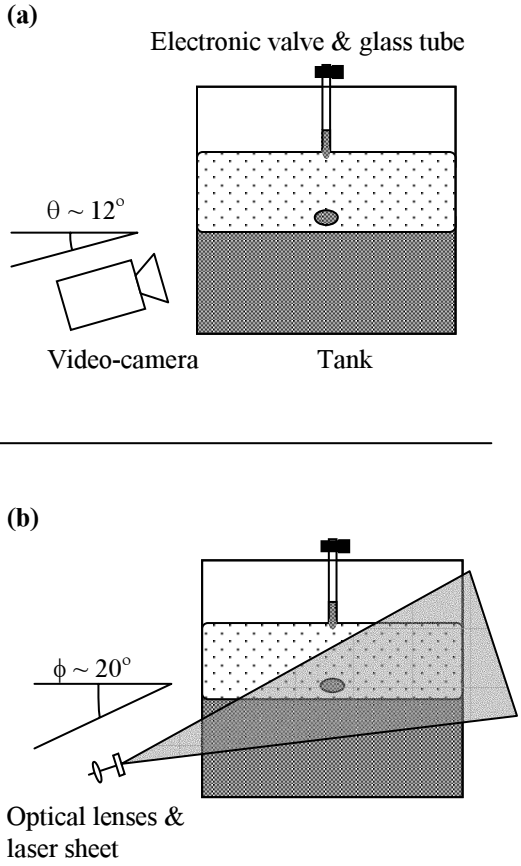

FIG. 1. Zulfaa Mohamed-Kassim, Physics of Fluids.

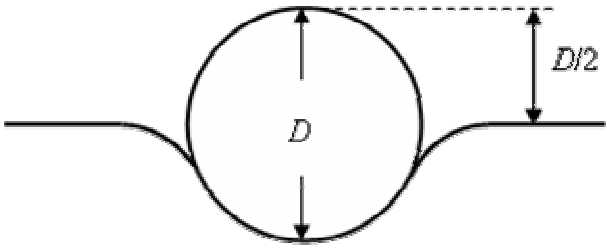

FIG. 2. Zulfaa Mohamed-Kassim, Physics of Fluids.

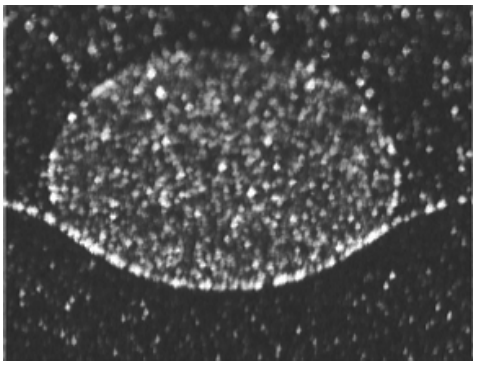

(a) t/t_σ = -0.01

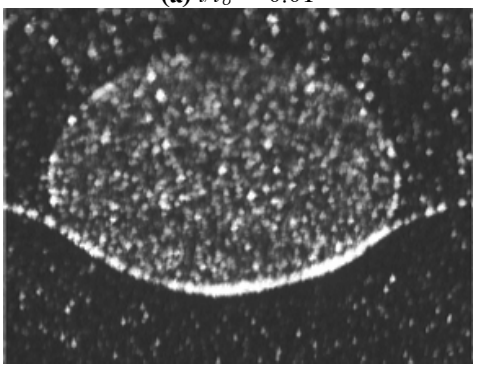

(b) t/t_σ = 0.0

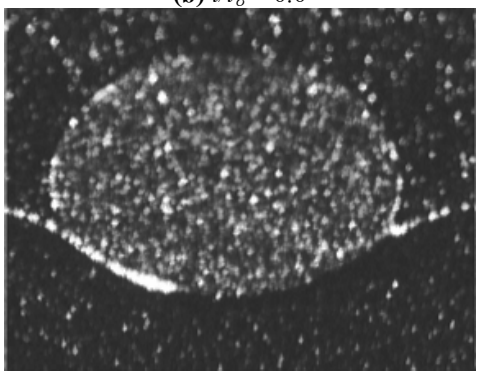

(c) t/t_σ = 0.01

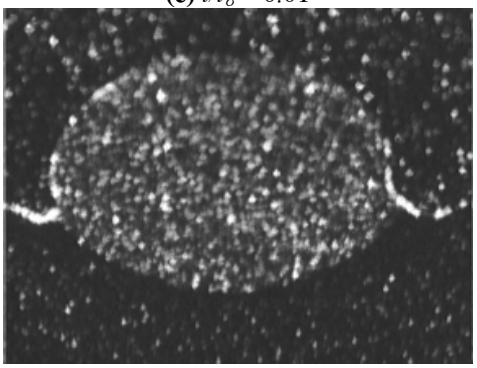

(d) t/t_σ = 0.04

FIG. 3. Zulfaa Mohamed-Kassim, Physics of Fluids.

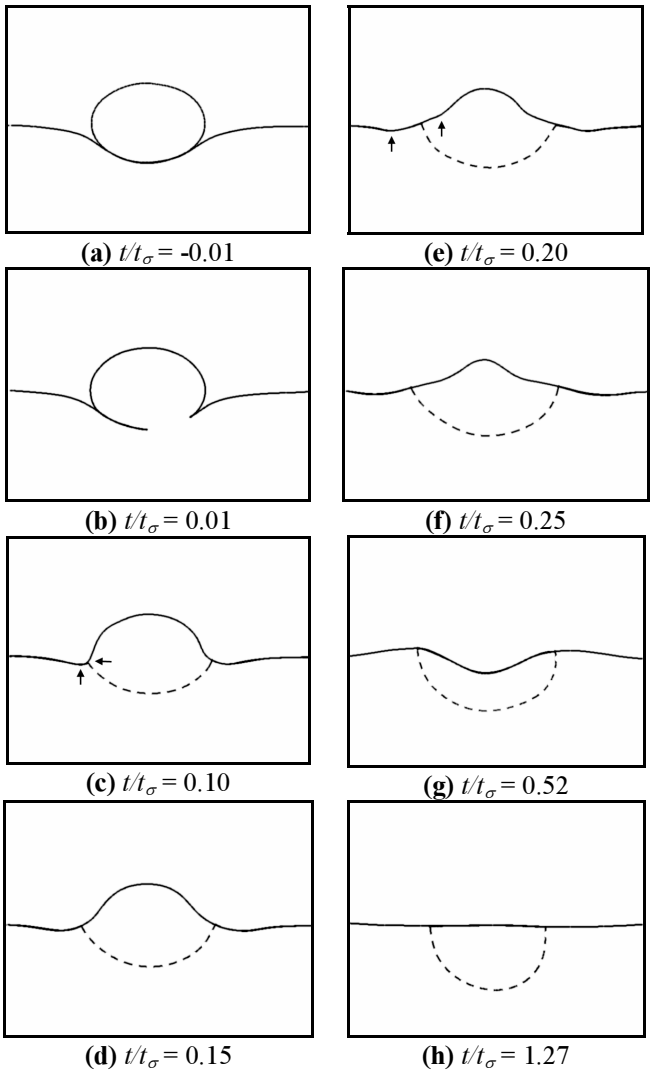

FIG. 4. Zulfaa Mohamed-Kassim, Physics of Fluids.

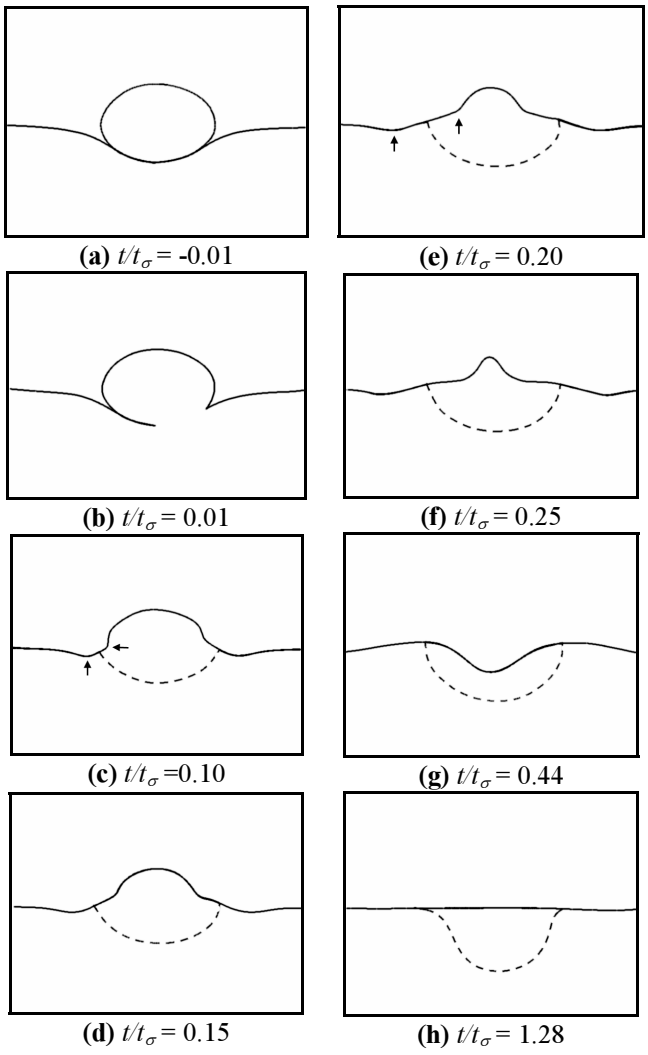

FIG. 5. Zulfaa Mohamed-Kassim, Physics of Fluids.

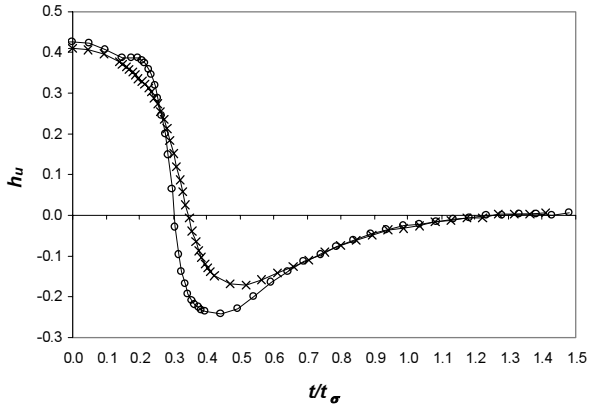

FIG. 6. Zulfaa Mohamed-Kassim, Physics of Fluids.

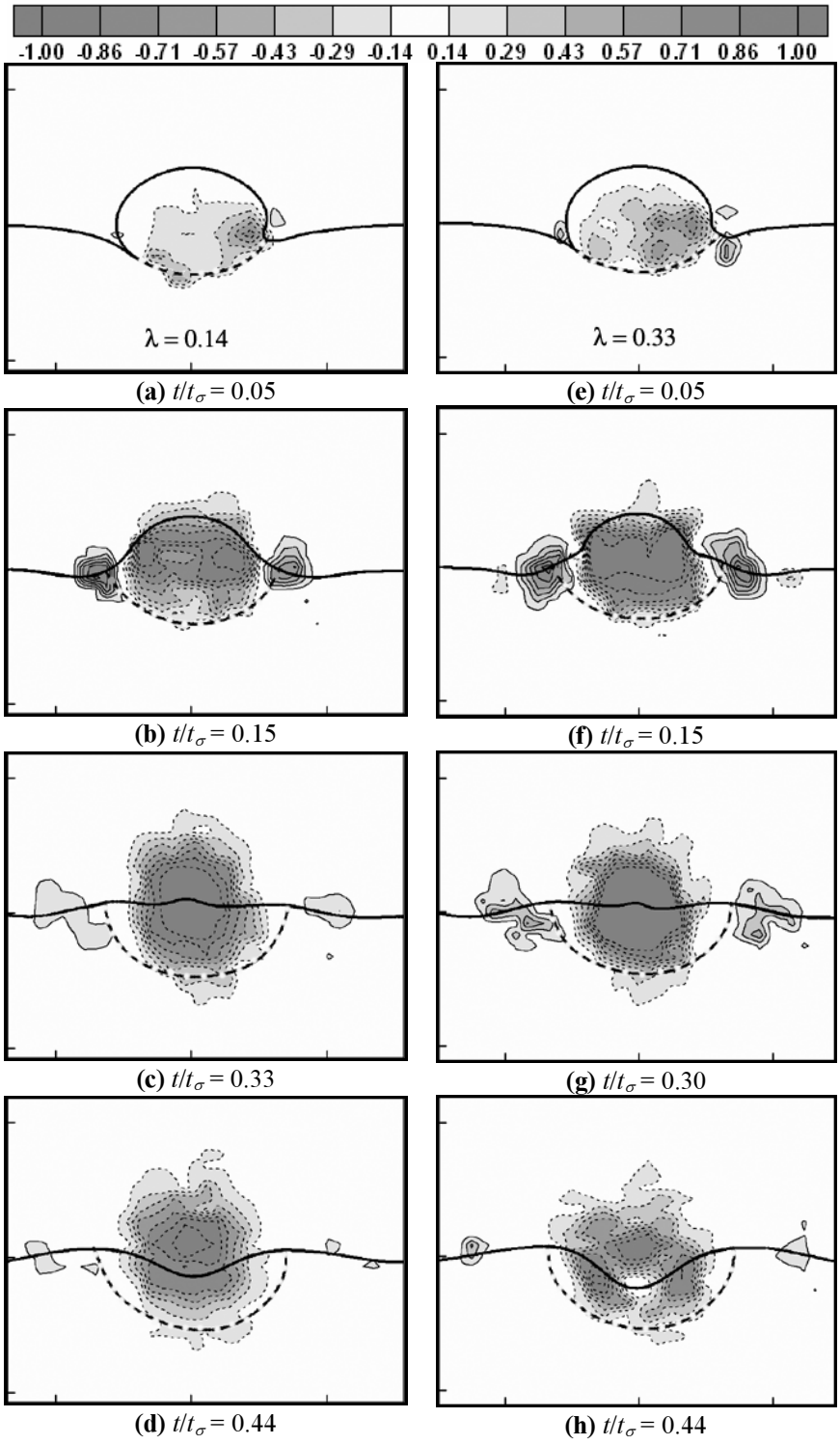

(a) $t/t_\sigma = 0.05$ **(e)** $t/t_\sigma = 0.05$

(b) $t/t_\sigma = 0.15$ **(f)** $t/t_\sigma = 0.15$

(c) $t/t_\sigma = 0.33$ **(g)** $t/t_\sigma = 0.30$

(d) $t/t_\sigma = 0.44$ **(h)** $t/t_\sigma = 0.44$

FIG. 7. Zulfaa Mohamed-Kassim, Physics of Fluids.

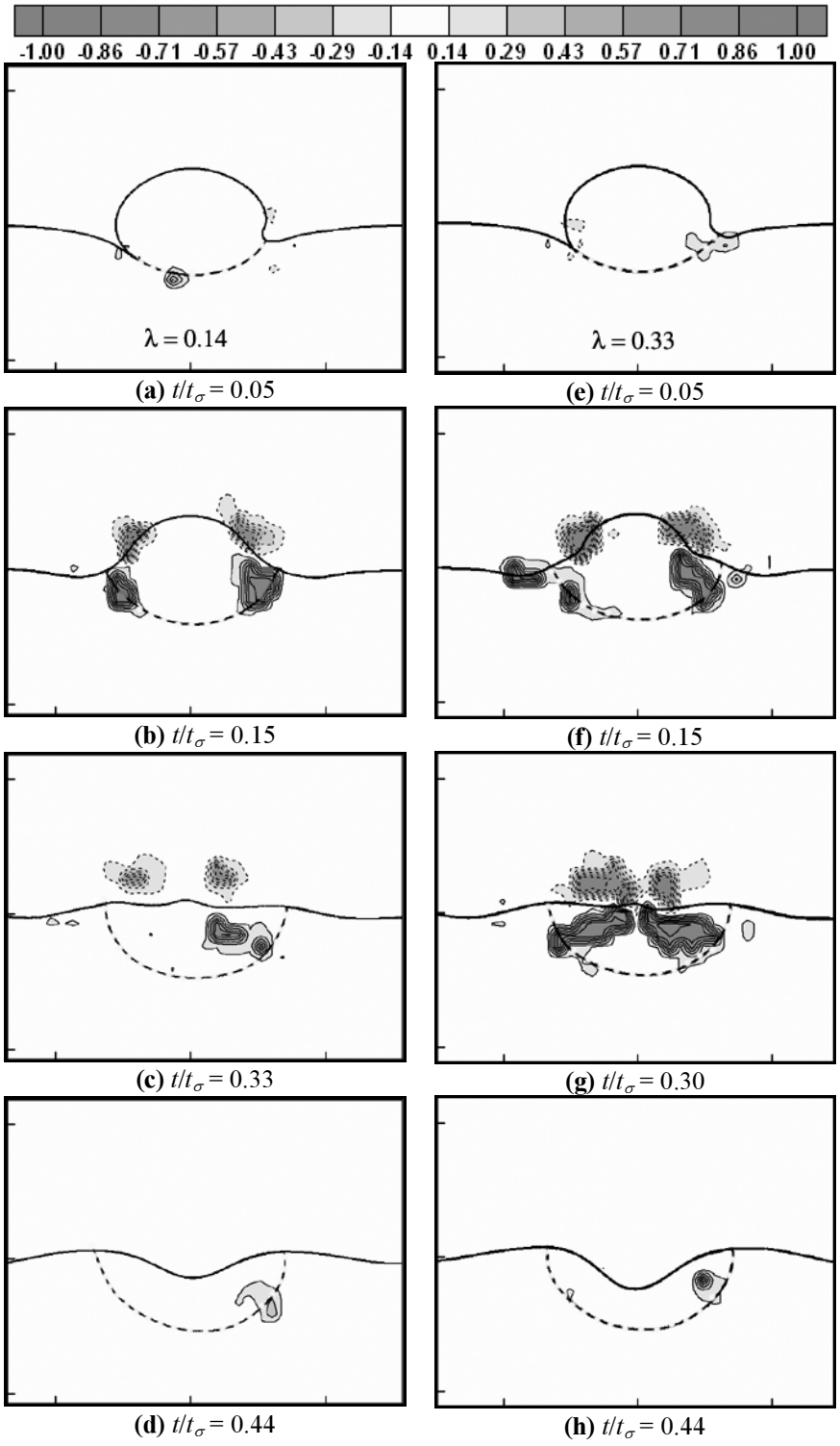

(a) $t/t_\sigma = 0.05$ **(e)** $t/t_\sigma = 0.05$

(b) $t/t_\sigma = 0.15$ **(f)** $t/t_\sigma = 0.15$

(c) $t/t_\sigma = 0.33$ **(g)** $t/t_\sigma = 0.30$

(d) $t/t_\sigma = 0.44$ **(h)** $t/t_\sigma = 0.44$

FIG. 8. Zulfaa Mohamed-Kassim, Physics of Fluids.

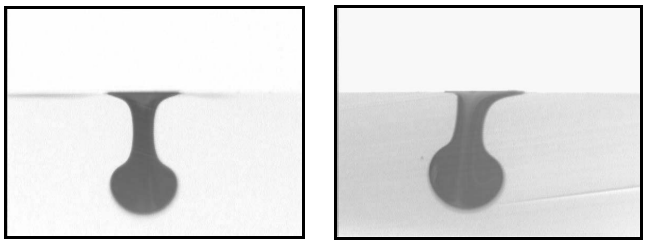

(a) $t/t_\sigma = 6.8$ **(b)** $t/t_\sigma = 6.2$

FIG. 9. Zulfaa Mohamed-Kassim, Physics of Fluids.

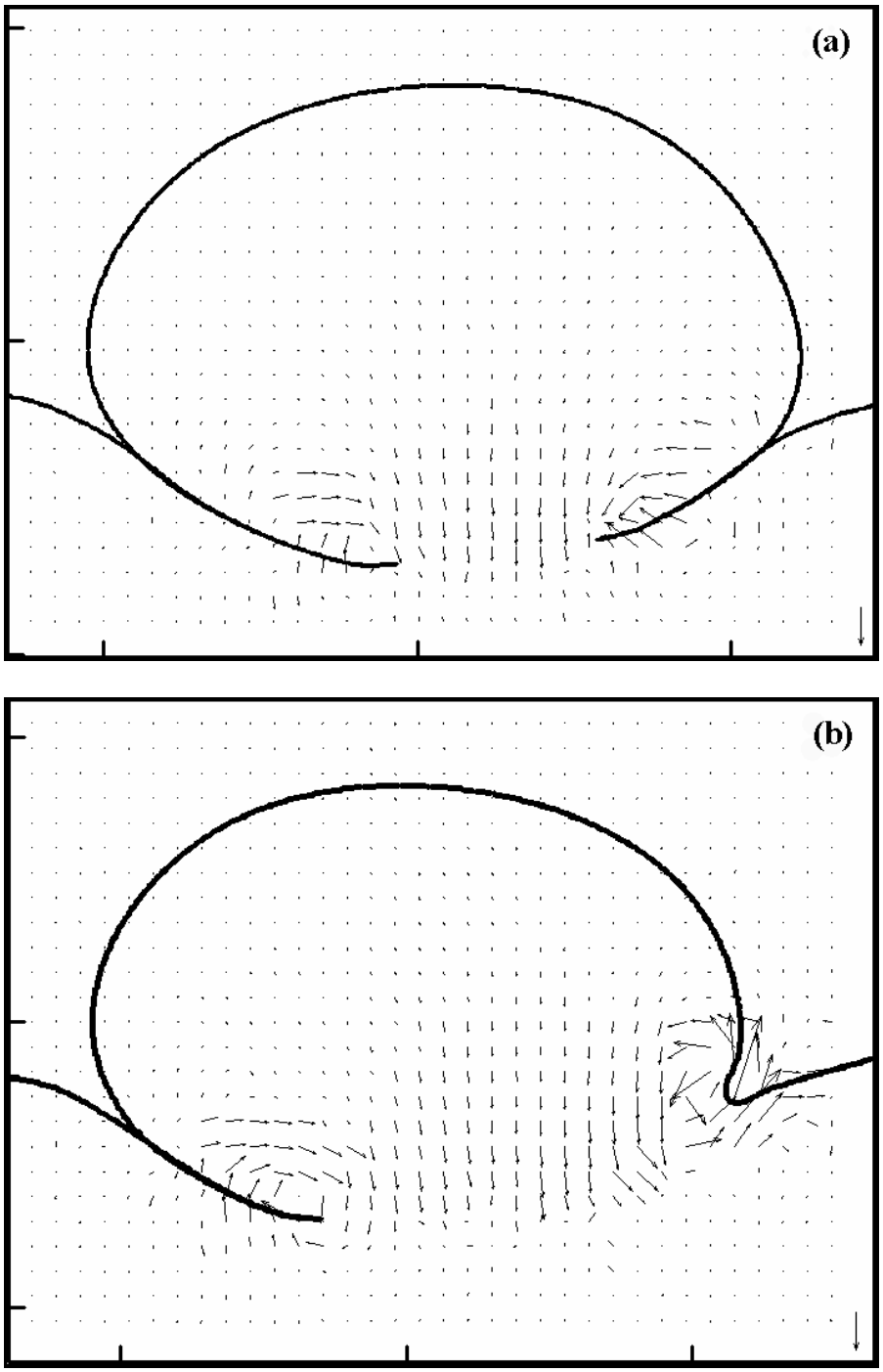

FIG. 10. Zulfaa Mohamed-Kassim, Physics of Fluids.

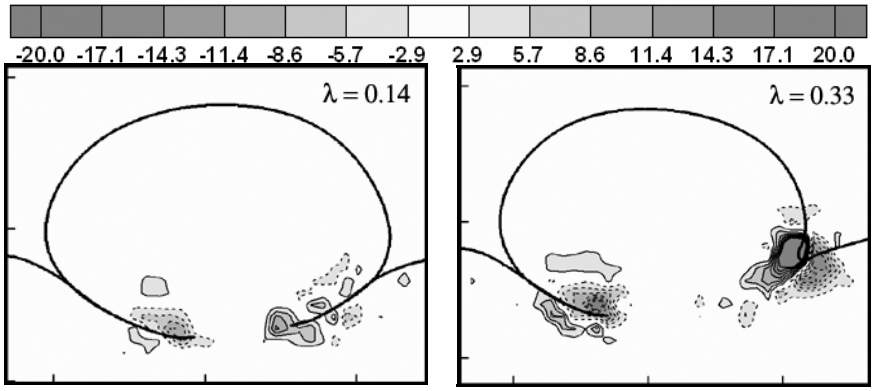

(a) $t/t_\sigma = 0.01$ **(b)** $t/t_\sigma = 0.01$

FIG. 11. Zulfaa Mohamed-Kassim, Physics of Fluids.

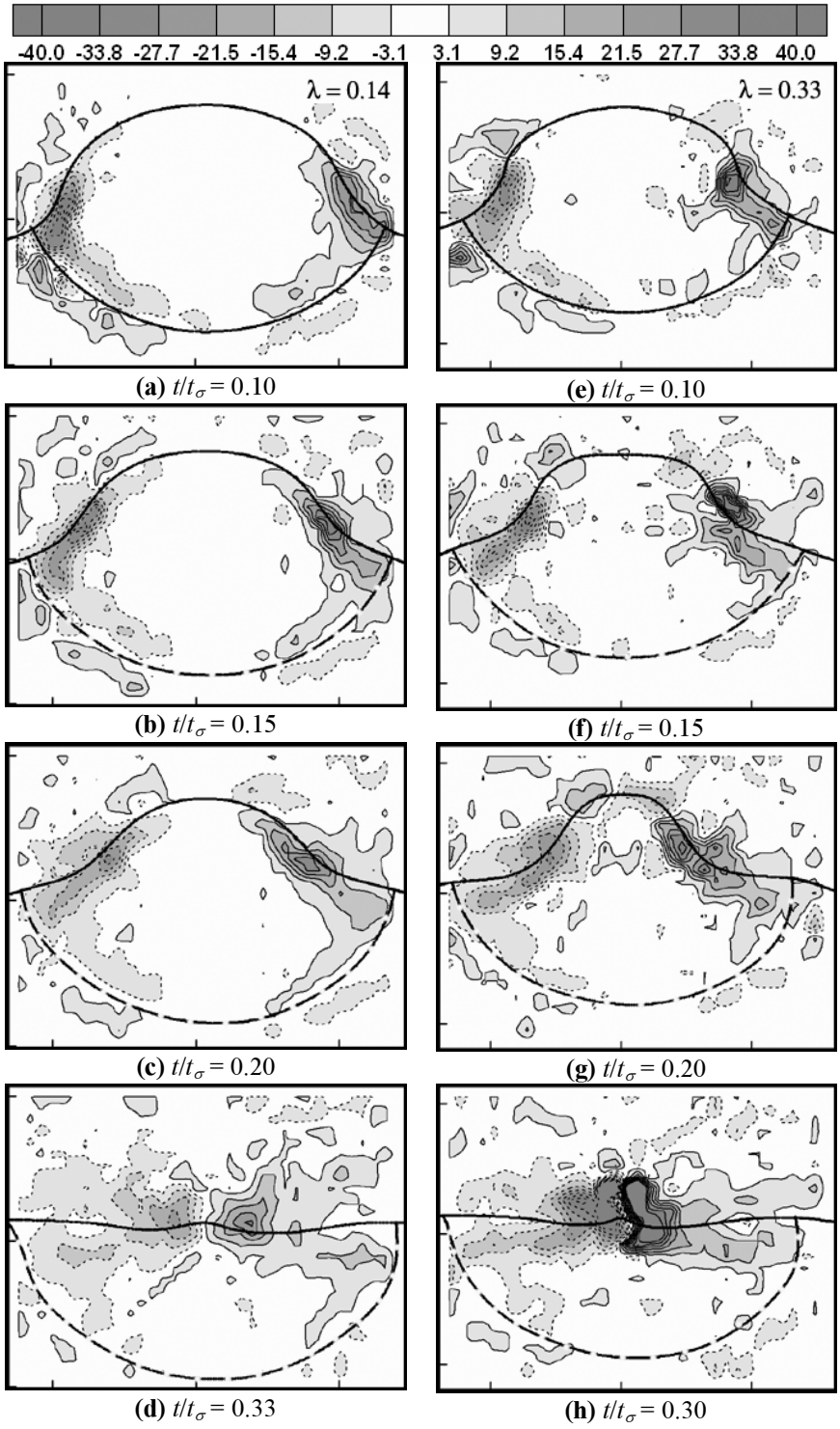

FIG. 12. Zulfaa Mohamed-Kassim, Physics of Fluids.

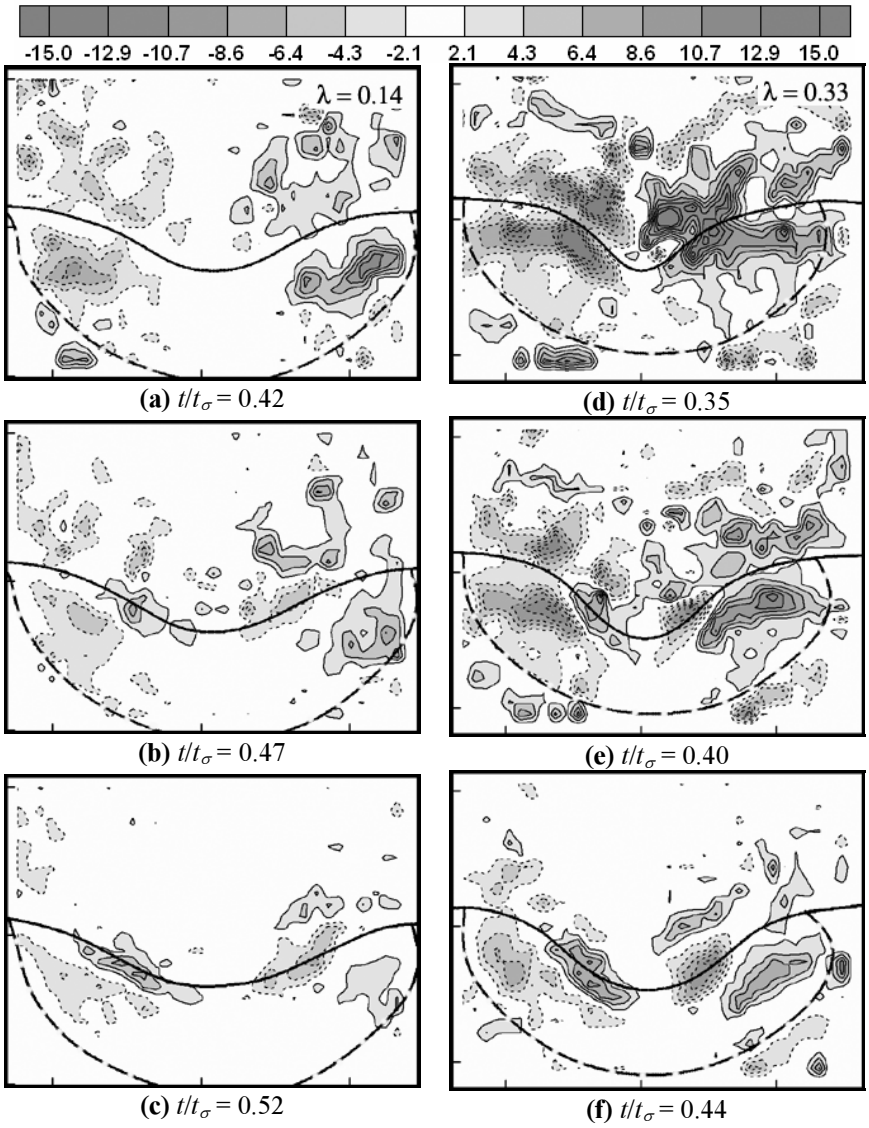

FIG. 13. Zulfaa Mohamed-Kassim, Physics of Fluids.